

# Lawrence Berkeley National Laboratory

## Lawrence Berkeley National Laboratory

### **Title**

Colloidally Synthesized Monodisperse Rh Nanoparticles Supported on SBA-15 for Size- and Pretreatment-Dependent Studies of CO Oxidation

### **Permalink**

<https://escholarship.org/uc/item/3n39v8cn>

### **Author**

Grass, Michael E.

### **Publication Date**

2009-05-15

Peer reviewed

# Colloidally Synthesized Monodisperse Rh Nanoparticles Supported on SBA-15 for Size- and Pretreatment- Dependent Studies of CO Oxidation

*Michael E. Grass,<sup>†§</sup> Sang Hoon Joo,<sup>†</sup> Yawen Zhang,<sup>†‡</sup> and Gabor A. Somorjai<sup>†\*</sup>*

<sup>†</sup> Department of Chemistry, University of California and Chemical and Materials Sciences Divisions,  
Lawrence Berkeley National Laboratory, Berkeley, California 94720

<sup>‡</sup> College of Chemistry and Molecular Engineering and State Key Lab of Rare Earth Materials  
Chemistry and Application and PKU-HKU Joint Lab in Rare Earth Materials and Bioinorganic  
Chemistry, Peking University, Beijing 100871, China

\*Corresponding author e-mail: somorjai@berkeley.edu

**RECEIVED DATE (to be automatically inserted after your manuscript is accepted if required  
according to the journal that you are submitting your paper to)**

TITLE RUNNING HEAD: PVP stabilized Rh nanoparticles for CO oxidation

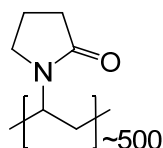
<sup>§</sup> Current Address: Advanced Light Source, Lawrence Berkeley National Laboratory, Berkeley,  
California 94720

A particle size dependence for CO oxidation over rhodium nanoparticles of 1.9 – 11.3 nm has been investigated and determined to be modified by the existence of the capping agent, poly(vinylpyrrolidone) (PVP). The particles were prepared using a polyol reduction procedure with PVP as the capping agent. The Rh nanoparticles were subsequently supported on SBA-15 during hydrothermal synthesis to produce Rh/SBA-15 supported catalysts for size-dependent catalytic studies. CO oxidation by O<sub>2</sub> at 40 Torr CO and 100 Torr O<sub>2</sub> was investigated over two series of Rh/SBA-15 catalysts: as-synthesized Rh/SBA-15 covering the full range of Rh sizes and the same set of catalysts after high temperature calcination and reduction. The turnover frequency at 443 K increases from 0.4 to 1.7 s<sup>-1</sup> as the particle size decreases from 11.3 to 1.9 nm for the as-synthesized catalysts. For the catalyst series after calcination and reduction, the turnover frequency is between 0.1 and 0.4 s<sup>-1</sup> with no particle size dependence. The apparent activation energy for all catalysts is ~ 30 kcal mol<sup>-1</sup> and is independent of particle size and thermal treatment. Infrared spectroscopy of CO on the Rh nanoparticles indicates that the heat treatments used influence the mode of CO adsorption. As a result, the particle size dependence for CO oxidation is altered after calcination and reduction of the catalysts. CO adsorbs at two distinct bridge sites on as-synthesized Rh/SBA-15, attributable to metallic Rh(0) and oxidized Rh(I) bridge sites. After calcination and reduction, however, CO adsorbs only at Rh(0) atop sites. The change in adsorption geometry and oxidation activity may be attributable to the interaction between PVP and the Rh surface. This capping agent affect may open new possibilities for the tailoring of metal catalysts using solution nanoparticle synthesis methods.

**KEYWORDS:** CO oxidation; Rh; poly(vinylpyrrolidone); SBA-15; size dependent catalysis

## 1. Introduction

A new class of catalysts has been developed over the past few decades that employs metal nanoparticles synthesized by colloidal methods.<sup>1</sup> Colloidal nanoparticles are typically synthesized by the reduction of metal salts in the presence of stabilizing or capping materials, often organic surfactants and/or polymers. Many studies have been undertaken to elucidate the catalytic properties of these metal nanoparticles (NPs), both in solution and deposited on solid supports.<sup>2-15</sup> One of the advantages of this method of catalyst preparation is the control of particle size that can be achieved. Colloidal routes to the formation of nanoparticles for supported catalysts give rise to a much narrower particle size distribution (PSD) than do traditional catalyst preparation methods, such as wetness impregnation or ion exchange. An additional benefit of colloidal nanoparticle syntheses for catalytic applications is the ability to systematically tune particle size and shape, as well as the composition of multi-element particles. An important question regarding these materials, however, is what affect the capping agents have on catalytic performance. This question has been addressed for solution phase catalysis by a few studies<sup>11,16</sup> and our group has studied the interaction of poly(vinylpyrrolidone) (PVP) (scheme 1) with supported Pt and Rh NPs in the gas phase.<sup>17,18</sup> The decomposition of PVP on Pt NPs in N<sub>2</sub> has also been studied,<sup>19</sup> but its affect on catalytic properties in gas phase reactions is not yet understood.



There are a limited number of studies involving the use of PVP protected metal nanoparticles supported on oxides for gas phase catalysis. Our group has used PVP protected Pt nanoparticles for hydrogenation reactions after a high temperature oxygen pretreatment and assumed that the PVP was completely removed during calcination at 623 – 723 K in flowing O<sub>2</sub>.<sup>9,20</sup> Venezia, *et al.* studied PVP protected Au/Pd bimetallic NPs supported on SiO<sub>2</sub> for CO oxidation and concluded that calcination at 673 K in air completely removed PVP.<sup>12</sup> Einaga, *et al.* immobilized PVP stabilized Pt NPs on TiO<sub>2</sub> and also used O<sub>2</sub> calcined at 673 K to remove PVP; IR spectroscopy of the catalysts during the calcination treatment indicate that the C=O stretch of PVP is greatly diminished by calcination at 673 K.<sup>21</sup>

Recently we demonstrated that PVP has no deleterious effects on room temperature ethylene hydrogenation by Pt NPs when no pretreatment is employed.<sup>22,23</sup> Ma *et al.* compared various Pt/zeolite catalysts with and without PVP for conversion of methane to higher hydrocarbons and found that catalytic performance was unaffected by PVP, although PVP electronically shields the Pt NPs from the support.<sup>24</sup> It is clear from numerous studies that PVP does not completely block catalytic activity in gas phase reactions, but its role in modifying catalytic activity has not been fully examined.

CO oxidation is an excellent benchmark reaction because it has been extensively examined over both model and technical catalysts. Many investigations of CO oxidation over Rh catalysts have been carried out, including studies with single crystals,<sup>25-29</sup> supported catalysts,<sup>29-37</sup> and model catalysts in which Rh NPs are supported on a flat oxide substrate.<sup>38-42</sup> The dependence of the rate of CO oxidation on the size of Rh NPs is not entirely understood. This is partly due to the fact that many studies of CO oxidation have been performed under widely varying catalytic conditions and with samples prepared using different synthetic methods. In two studies of CO desorption from model Rh NP catalysts, it was found that CO desorbs at a lower temperature from smaller NPs.<sup>38,41</sup> CO oxidation at low pressures over O-precovered Rh surfaces is structure sensitive, with Rh(100) being more active than Rh(111)<sup>27</sup> and smaller particles more active than larger particles.<sup>40</sup> At higher pressures, steady state measurements of CO oxidation in a 1:1 mixture of CO and O<sub>2</sub> demonstrated no structure sensitivity over supported Rh NP catalysts or Rh single crystals.<sup>29,34,35</sup>

In a recent study, we reported that smaller PVP capped Rh NPs are more active for CO oxidation at low temperature and with an O<sub>2</sub>/CO ratio of 2.5. For that investigation, we studied Rh NPs with *in situ* XPS and correlated the surface state of Rh with catalytic activity.<sup>43</sup> In order to further develop our understanding of the size-dependent activity for these NPs, we have supported the same NPs on high surface area mesoporous silica. This preparation allowed us to perform various high temperature pretreatments before catalytic measurements, as well as to perform additional analytical methods such as selective gas adsorption and infrared spectroscopy. In light of these new investigations, we propose a model for PVP-induced particle size dependence of CO oxidation over Rh NPs between 2 and 12 nm.

## 2. Experimental

### 2.1 Synthesis and Characterization of Rh Nanocrystals

Rhodium(III) acetylacetonate, 1,4-butanediol (99%; bp 503 K), poly(vinylpyrrolidone) (PVP,  $MW = 55,000$ ), and sodium citrate were purchased from Sigma-Aldrich. All solvents except 1,4-butanediol, including acetone, ethanol, and hexanes, were of analytical grade and used without further purification. 1,4-butanediol was dried with a molecular sieve for at least two days before use to reduce water contamination.

A series of Rh nanoparticles (NPs) in the range of 1.9 – 11.3 nm were synthesized following the one-step polyol synthesis method described previously.<sup>43,44</sup> The size of Rh NPs was controlled by varying the concentrations of Rh(acac)<sub>3</sub> and sodium citrate. Smaller Rh NPs (1.9, 2.4, 3.6, and 5.1 nm) were synthesized in the presence of sodium citrate while larger NPs (6.7 and 11.3 nm) were prepared without sodium citrate. For the synthesis of Rh(1.9 nm), 80.0 mg of Rh(acac)<sub>3</sub>, 222 mg of PVP, and 58.8 mg of sodium citrate (2 mmol) were added to 40 mL of 1,4-butanediol in a 100 mL three-necked flask at room temperature. The reaction mixture was heated to 413 K under vacuum and was further evacuated at this temperature with continuous stirring for 20 min to remove water and oxygen. The mixture was then heated to 493 K at a rate of 10 K min<sup>-1</sup> and maintained at this temperature for 2 h under Ar. At the completion of the reaction, excess acetone was added after allowing the mixture to cool to room temperature, forming a cloudy black suspension. This suspension was separated by centrifugation and the particles were collected by discarding the colorless supernatant. The precipitated Rh NPs were washed with acetone and redispersed in ethanol. The other Rh NPs were synthesized using the same protocol, but with varying reagent concentrations and temperatures. The experimental conditions and corresponding sizes of Rh NPs are summarized in Table 1.

Particle size was analyzed using a Philips FEI Tecnai 12 transmission electron microscope (TEM) operated at 100 kV. X-ray diffraction (XRD) patterns were recorded on a Bruker D8 GADDS diffractometer with Co K<sub>α</sub> radiation ( $\lambda = 1.79 \text{ \AA}$ ).

### 2.2 Catalyst Synthesis and Characterization

Pluronic P123 (EO<sub>20</sub>PO<sub>70</sub>EO<sub>20</sub>, BASF), tetramethyl orthosilicate (TMOS, 98%, Aldrich), and sodium fluoride (99.99%, Aldrich) were used as received.

Rh(*X*)/SBA-15 catalysts (*X* = 1.9, 2.4, 3.6, 5.1, 6.7, or 11.3 nm) were synthesized by nanoparticle encapsulation (NE).<sup>20</sup> 2.5 g of Pluronic P123 was completely dissolved in 50.5 mL deionized water and added to an aqueous solution of Rh NPs (27.0 mL, 5.9 mM based on total Rh). This solution was stirred for 1 h at 313 K followed by addition of 0.38 mL of 0.5 M aqueous NaF and 3.9 mL TMOS and additional stirring for 20 h at 313 K. The reaction mixture was further aged for 24 h at 373 K in a closed vessel. The precipitates were separated by centrifugation, thoroughly washed with DI water and ethanol, and dried at room temperature for 2 days. The resulting samples are designated Rh(*X*)/SBA-15, where *X* denotes the size of the Rh NPs determined by TEM. In order to test the effect of high temperature O<sub>2</sub> calcination, a fraction of each sample was pretreated in 100 mL min<sup>-1</sup> O<sub>2</sub> at elevated temperature. Rh(1.9 nm)/SBA-15 and Rh(2.4 nm)/SBA-15 samples were calcined at 623 K for 24 h, Rh(3.6 nm)/SBA-15 and Rh(5.1 nm)/SBA-15 were calcined at 723 K for 24 h, and Rh(6.7 nm)/SBA-15 and Rh(11.3 nm)/SBA-15 were calcined at 723 K for 36 h. These samples are denoted Rh(*X*)/SBA-15-c.

Both the calcined and uncalcined catalysts were analyzed by TEM and XRD. Additionally, the Rh content was determined by inductively coupled plasma optical emission spectroscopy (ICP-OES) (Mikroanalytisches Labor Pascher) and electron probe microanalysis (EPMA). Rh loadings measured by EPMA were between 4% and 12% higher than measured by ICP-OES for all samples. Active metal surface area was determined by room temperature adsorption of H<sub>2</sub> and CO using a Quantachrome Autosorb-1 automated sorption analyzer. ~ 200 mg of a Rh(*X*)/SBA-15-c catalyst was loaded into a quartz cell and reduced *in situ* at 623 K for 1.5 h in flowing H<sub>2</sub> followed by evacuation of the sample at 623 K for 1 h. The sample was then cooled in vacuo to 303 K for sorption measurements with H<sub>2</sub> (Praxair, 99.999%) or CO (Praxair, 99.99%). As-synthesized Rh(*X*)/SBA-15 samples were additionally characterized using combined thermogravimetric analysis and differential temperature analysis (TGA-

DTA; TA Instruments SDT 2960) by heating from room temperature to 1273 K at a rate of 10 K min<sup>-1</sup> or 5 K min<sup>-1</sup> in a flow of pure O<sub>2</sub> at 100 mL min<sup>-1</sup>.

### **2.3 CO Oxidation measurements**

Catalytic measurements were carried out in a home built Pyrex reaction system operated as a plug flow reactor.<sup>9</sup> Flow rates of oxygen (Praxair, 99.995%), carbon monoxide (Praxair, 99.99%), and helium (Praxair, 99.999%) were controlled using mass flow controllers (Porter Instruments) and reactants and products were analyzed by gas chromatography (HP 5890 Series II). In a typical experiment, 20 – 120 mg of catalyst was mixed with acid washed and calcined quartz sand. The reactor was purged with He and heated to 373 K in flowing He for 1 h. A flow rate of 80 mL min<sup>-1</sup> consisting of 40 Torr CO, 100 Torr O<sub>2</sub>, and a background of He was then established at room temperature and the sample was heated to the desired reaction temperature (403 – 503 K). For the calcined samples, an *in situ* 1 hr reduction in 100 Torr H<sub>2</sub>/He (80 mL min<sup>-1</sup>) at 623 K preceded the reaction studies.

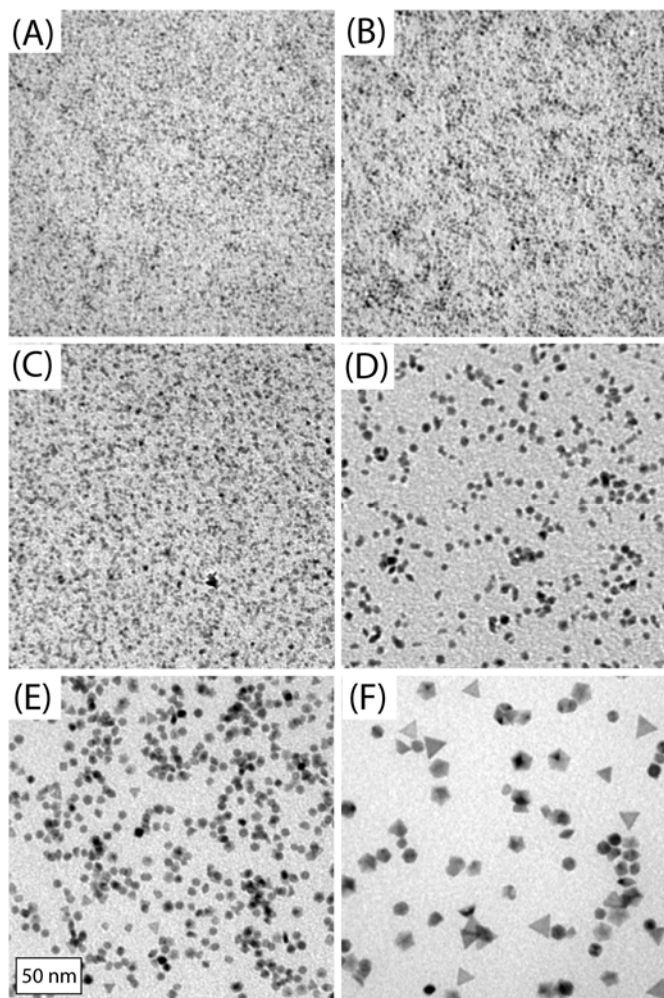
### **2.4 Diffuse Reflectance Infrared Spectroscopy of CO on Rh/SBA-15**

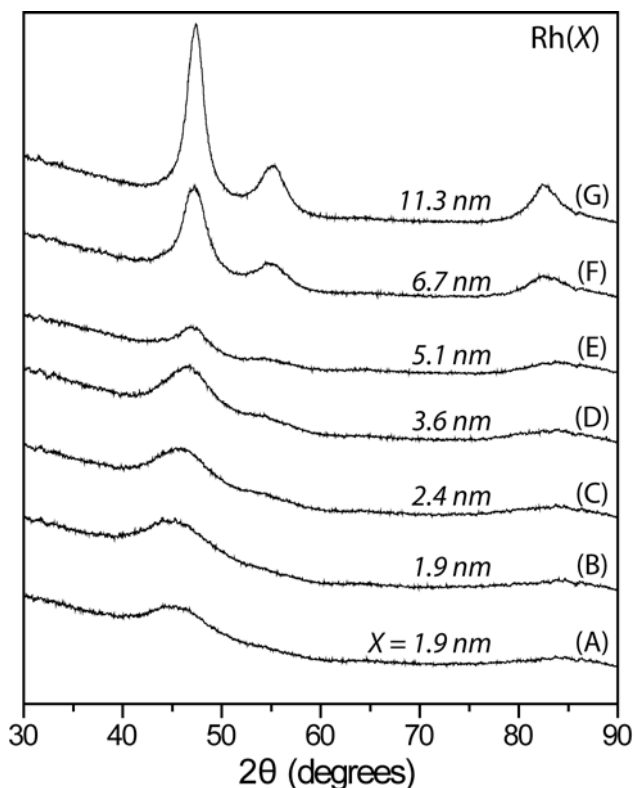
Diffuse reflectance FTIR spectroscopy (DRIFTS) was used to investigate the adsorption of CO on Rh(X)/SBA-15 catalysts as-synthesized, after calcination, and following a subsequent reduction in H<sub>2</sub> at 573 K. Experiments were conducted with a Nicolet Nexus 670 spectrometer equipped with a Thermo Spectra-Tech controlled atmosphere-diffuse reflectance cell. For studies of as-synthesized samples (Rh(X)/SBA-15), ~ 7 mg of sample was loaded into the diffuse reflectance cell and purged at 393 K in N<sub>2</sub> (80 mL min<sup>-1</sup>) to remove gas-phase and weakly bound water. The samples were cooled and then exposed to 1% CO/He (30 mL min<sup>-1</sup>) for 5 min followed by a 50 min N<sub>2</sub> purge. Reported spectra of CO exposed catalysts have had a background subtraction. For the study of calcined samples (Rh(X)/SBA-15-c), the calcination was performed *ex situ* as described above, and the sample was treated in the same way as the as-synthesized samples in the DRIFTS cell. For calcined and reduced samples, an *in situ* reduction was carried out on Rh(X)/SBA-15-c at 573 K in 10% H<sub>2</sub>/He (30 mL min<sup>-1</sup>) for 1 h followed by a 30 min N<sub>2</sub> purge (80 mL min<sup>-1</sup>) at the same temperature. All spectra are an average of 256 scans at 4 cm<sup>-1</sup> resolution.

### 3. Results and Discussion

#### 3.1 Synthesis and Characterization of Rh Nanoparticles

The synthesis and characterization of Rh NPs in the size range 1.9 – 13.5 nm has been reported previously.<sup>43,44</sup> TEM images (Figure 1) and XRD patterns (Figure 2) for these samples are consistent with our previous work,<sup>43,44</sup> although the exact particle size from a given preparation varies slightly. The particle size and standard deviation from an analysis of 200 particles via TEM are listed in the final column of Table 1. The larger well faceted particles (>5 nm; Figure 1d-f) have predominately exposed (111) crystal planes.<sup>44</sup> The XRD patterns show a broadening of the peaks along with a shift to lower  $2\theta$ , consistent with the Scherer equation and a relaxation of the Rh-Rh bond distance in smaller particles. This relaxation is  $\sim 5\%$  as the particle size decreases from 11.3 to 1.9 nm. The measured crystallite size by the Scherer equation is smaller than the particle size observed by TEM, which is expected because a significant fraction of the particles are {111} twinned particles with grain boundaries.<sup>44</sup>





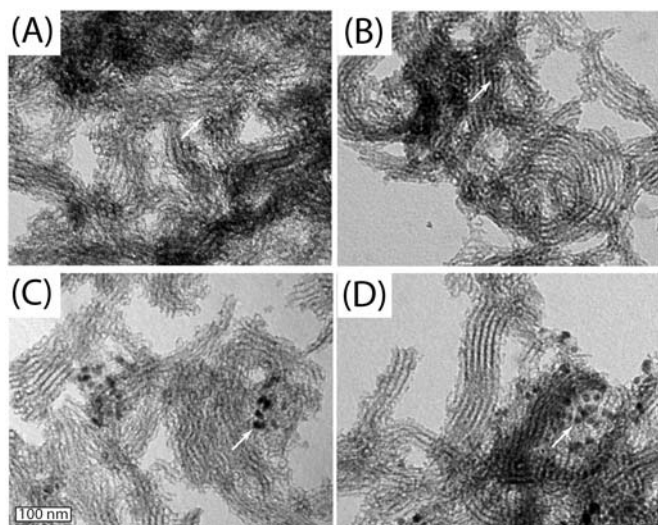
### 3.2 Synthesis and Characterization of Rh/SBA-15 Catalysts

The Rh/SBA-15 catalysts have been characterized by elemental analysis, XRD, TEM, TGA-DTA, and H<sub>2</sub> and CO chemisorption. Elemental analysis and TEM were performed after the samples were calcined, XRD was measured before and after calcination, and chemisorption was performed after calcination and an *in situ* reduction. Table 2 contains a summary of the calcination protocols for all samples, the Rh loading measured by ICP-OES, and H/Pt and CO/Pt from H<sub>2</sub> and CO chemisorption. All samples were prepared with a nominal loading of 1% Rh by weight assuming 100% yield for the synthesis of the NPs and full incorporation in the preparation of the catalysts. The Rh loading data indicates that the overall yield for the NP synthesis and encapsulation is 50 – 90% with a typical preparation having ~ 80% yield, consistent with our previous work with Pt NPs.<sup>20</sup>

Rh dispersion from H<sub>2</sub> chemisorption is in relatively good agreement with the theoretical dispersion calculated from TEM measurements (Table 2). The H/Rh ratio is somewhat lower than the dispersion expected from TEM for all samples except Rh(11.3 nm)/SBA-15-c, which has a H/Rh ratio exactly matching the theoretical dispersion from TEM. One notable exception is Rh(5.1 nm)/SBA-15-c, for which the H/Rh ratio (0.13) is significantly lower than the theoretical dispersion (0.24). CO

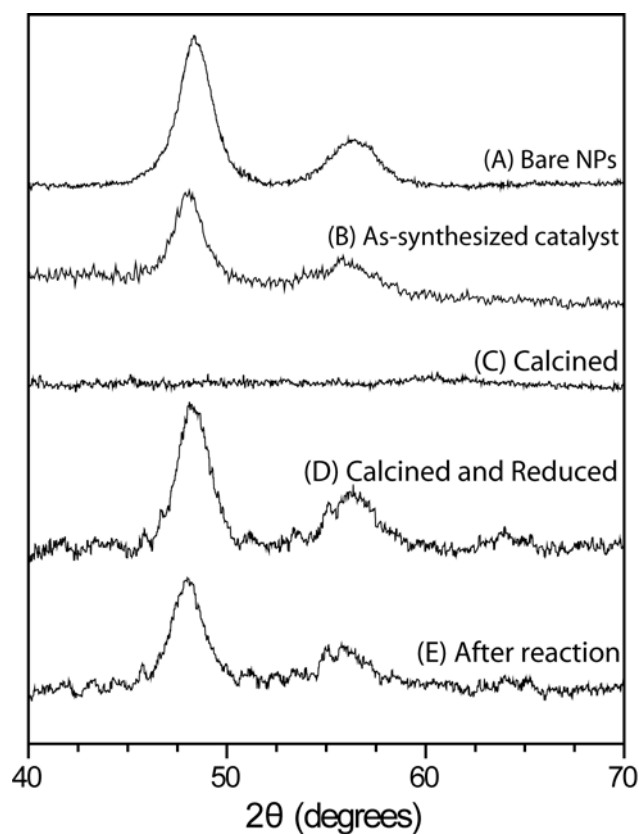
chemisorption measurements also indicate lower dispersion than calculated from TEM. The CO/Rh ratio is lower than the theoretical dispersion calculated from TEM by a factor of 0.3 – 0.5 for most samples, with the outlier again being the Rh(5.1 nm)/SBA-15 catalyst with a CO/Rh ratio of 0.02 and a theoretical dispersion of 0.24. The lower H/Rh ratios relative to TEM analysis may be the result of blocked sites from decomposed PVP or P123 in the calcination and reduction procedure. Particle sintering is another possibility, though there is no evidence for this in TEM. The CO/Rh ratios may also be affected by the adsorption of CO at bridge sites or three-fold sites, which would decrease the CO/Rh ratio for a given Rh dispersion. The outlying data of the Rh(5.1 nm)/SBA-15-c sample is not understood, and we take this into account when analyzing the reactivity data from this catalyst.

TEM analysis of Rh(X)/SBA-15-c (Figure 3) reveals that the NPs do not aggregate in the nanoparticle encapsulation or calcination procedures, but the larger particles do tend to deposit in the support as clusters of particles, as previously observed.<sup>22</sup> Particle size distribution analysis of the Rh(X)/SBA-15 catalysts is consistent with the particle size distribution obtained for NPs before encapsulation.



XRD peaks are only observed for samples with larger NPs and thus sharper diffraction peaks (Rh(6.7 nm)/SBA-15, Rh(11.3 nm)/SBA-15) after encapsulation in SBA-15. The diffraction peaks appear at the same position and have the same FWHM as for the colloiddally prepared particles before encapsulation (Figure 4A and B), but completely disappear after calcination (before subsequent reduction) (Figure 4C). It appears that the calcination protocol (Table 2) causes the formation of a non-

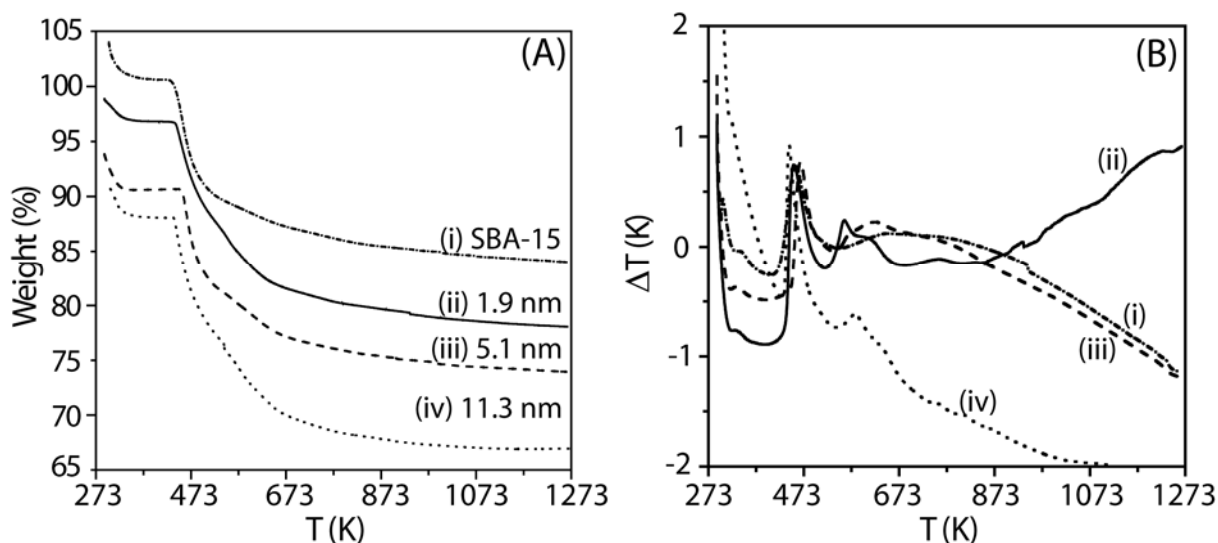
crystalline Rh oxide, as no diffraction peaks from Rh or Rh oxide are observed. It cannot be determined if the entire particle oxidizes or if a small Rh(0) core remains. As mentioned, no Rh peaks are observed for Rh(*X*)/SBA-15 catalysts where *X* < 6.7 nm, so that even an oxide of modest thickness could result in the absence of diffraction peaks for Rh(6.7 nm)/SBA-15-c and Rh(11.3 nm)/SBA-15-c. After reduction in H<sub>2</sub> at 623 K for 1 h and/or CO oxidation at ~ 473 K, the diffraction peaks are restored, indicating that the particles are (mostly) reduced under such conditions (Figures 4D and E). The oxidation state of the Rh NPs during reaction was the subject of a previous study.<sup>43</sup>



The weight loss of the as-synthesized catalysts was analyzed by TGA-DTA in flowing O<sub>2</sub> (Figure 5). At low temperatures (< 373 K), there is an initial weight loss of ~ 4% corresponding to the loss of water. A second weight loss event begins at ~ 438 K and corresponds to combustion of the templating surfactant, P123. This weight loss accounts for an additional 16 – 18% mass loss and is accompanied by an exotherm at the onset. The temperature of the blank SBA-15 and all Rh(*X*)/SBA-15 samples except Rh(11.3 nm)/SBA-15 increases by < 1 K relative to an inert reference at a heating rate of 10 K min<sup>-1</sup> and the weight loss profiles are similar to those shown in Figure 5 for Rh(1.9 nm)/SBA-

15 and Rh(5.1 nm)/SBA-15. The sample Rh(11.3 nm)/SBA-15 underwent extremely rapid weight loss accompanied by a 35 K exotherm when heated at 10 K min<sup>-1</sup>. For this reason, the experiment was repeated at 5 K min<sup>-1</sup>, shown in Figure 5. The main difference between Rh(11.3 nm)/SBA-15 and the remaining samples is that the NPs are larger than the size of the mesopores of the support (~ 10 nm). It is thus possible that the particles partially block the pores and combustion occurs very rapidly at the higher heating rate. We have observed a similar phenomenon for Pt(9.1 nm)/SBA-15 catalysts during temperature programmed reduction (unpublished data) and further study of this process may be warranted.

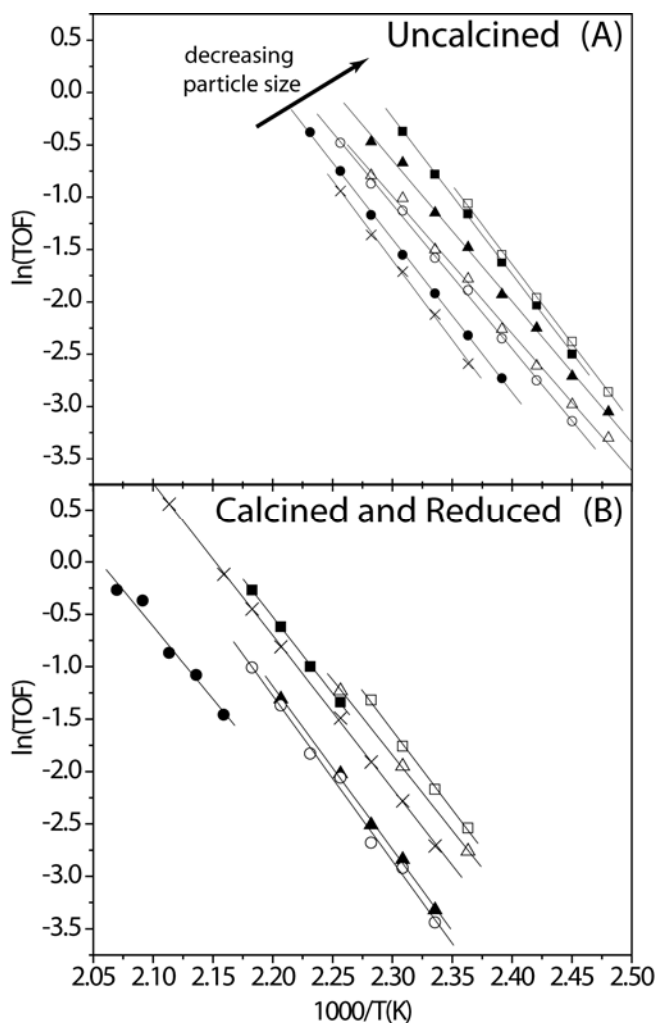
A second smaller exotherm is observed at ~ 550 K corresponding to the temperature at which PVP decomposes over 1.7 nm Pt NPs (not loaded on a support) using the same TGA-DSC protocol.<sup>45</sup>



### 3.3 CO Oxidation

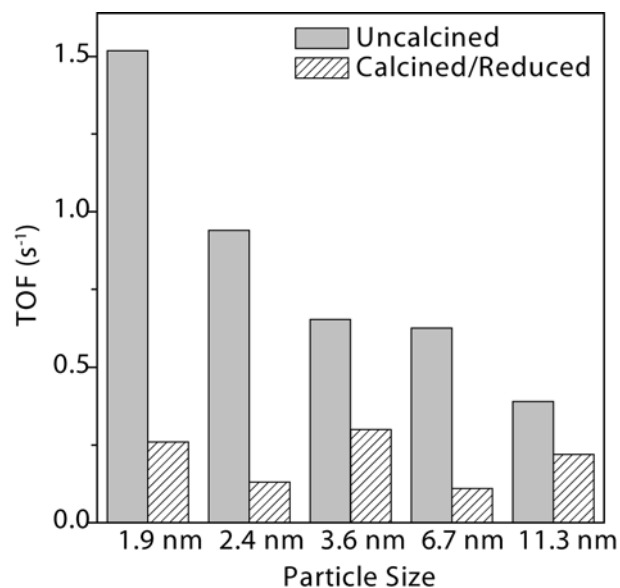
All catalysts were tested for CO oxidation activity at pressures of 40 Torr CO and 100 Torr O<sub>2</sub> and at temperatures below the ignition temperature, which ranged between 440 and 500 K depending on the catalyst, the pretreatment, and the amount loaded. The TOF was calculated based on TEM measurements assuming spherical particles. Arrhenius plots for CO oxidation are shown in Figure 6 and the apparent activation energy and TOF at 443 K are summarized in Table 3. Data is given separately for the as-synthesized samples (Rh(X)/SBA-15) and the calcined and reduced samples

(Rh(X)/SBA-15-c). A few general trends are readily observed. The activation energy for CO oxidation is  $\sim 30 \text{ kcal mol}^{-1}$  for each catalyst and there is no trend in the activation energy as a function of either particle size or pretreatment. The CO and O<sub>2</sub> reaction orders were tested for selected catalysts (not shown) and agreed with literature steady state measurements taken at similar pressures and temperatures – the reaction orders were approximately +1 in O<sub>2</sub> and –1 in CO for all catalysts.



From the TOF at 443 K listed in Table 3 and shown graphically in Figure 7, a few clear trends emerge. The uncalcined samples (Rh(X)/SBA-15) are more active than the calcined and reduced samples (Rh(X)/SBA-15-c). The TOF for Rh(11.3 nm)/SBA-15 decreases by a factor of 1.8 upon calcination and all other catalysts suffer a loss in specific activity greater than this after calcination and reduction. The largest decrease in TOF is found for Rh(2.4 nm)/SBA-15, for which the TOF decreases by a factor of 7.3, from  $0.94 \text{ s}^{-1}$  for the as-synthesized catalyst to  $0.13 \text{ s}^{-1}$  after calcination and reduction

at 443 K (Table 3). The decrease in catalytic activity after calcination and reduction is discussed further in light of IR spectroscopy investigations of CO adsorbed on these catalysts in section 3.5.



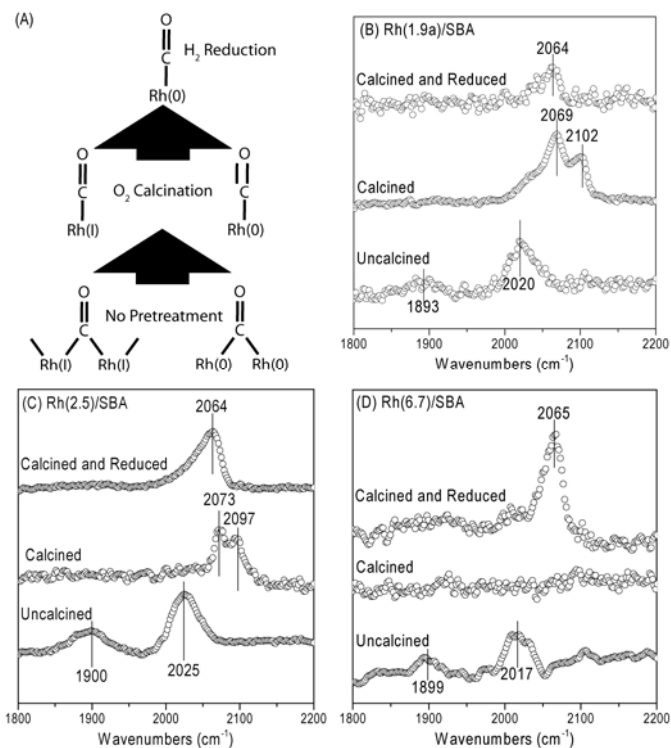
The TOF increases monotonically with decreasing particle size from  $0.39 \text{ s}^{-1}$  for Rh(11.3 nm)/SBA-15 to  $1.69 \text{ s}^{-1}$  for Rh(1.9 nm)/SBA-15 for the catalysts that have not been calcined. This increase is demonstrated in an Arrhenius plot in Figure 6(A) and also in Figure 7. The particle size dependence observed for these catalysts is similar to the trend we observed in a previous study of similar NPs, which were deposited onto silicon wafers by Langmuir-Blodgett deposition.<sup>43</sup> CO oxidation studies of the LB films were performed in the same reactor and the samples were treated similarly to the as-synthesized Rh(X)/SBA-15 catalysts. In our work with LB films of these particles we observed that smaller particles are more readily oxidized during CO oxidation and attributed the observed size dependent TOF to this phenomenon. An increase in activity for CO oxidation with decreasing particle size for Pd NPs has recently been reported by Chen *et al.* and was also attributed to the fact that smaller NPs oxidize more easily.<sup>46</sup>

The initial deactivation of Rh(X)/SBA-15 and Rh(X)/SBA-15-c was examined by loading fresh catalyst sample into the reactor, purging with He at 373 K, then heating to 408 K in the presence of CO and O<sub>2</sub> as described above. The reaction temperature was increased in steps of either 5 or 10 K to 473 K, then the catalyst was cooled to 443 K and the reaction rate was measured in steps of 10 K again. At all temperatures, the reaction rate was stable and no deactivation was observed. The same experiment

was repeated for calcined and reduced Rh(11.3 nm)/SBA-15-c. The calcined catalyst was first reduced in a flow of 100 Torr H<sub>2</sub> at 623 K, then purged with He and cooled to 408 K for the start of the reaction. The reaction rate was monitored as the catalyst was heated in steps, but deactivation was observed at temperatures above 438 K. At this stage, the catalyst was heated to 473 K and the reaction was monitored until a steady state rate was observed and reaction rates were measured between 453 and 473 K. A large degree of deactivation occurs for the calcined-reduced sample, but not for the uncalcined sample.

### ***3.4 Diffuse Reflectance Infrared Spectroscopy***

In order to explore the change in particle size dependence observed for samples before and after high temperature calcination, we have studied the adsorption of CO on the NP surfaces before calcination, after calcination, and after calcination followed by *in situ* reduction. After pretreatment (if any) and an initial purging with N<sub>2</sub>, the sample was exposed to CO at room temperature, followed by purging CO with N<sub>2</sub> and then taking spectra. For the as-synthesized samples, peaks at ~1900 and ~2025 cm<sup>-1</sup> are clearly observed (Figure 8). After calcination, these peaks disappear while new peaks at ~2070 and ~2100 cm<sup>-1</sup> are observed. After reduction in H<sub>2</sub> at 573 K, only the peak at ~2070 cm<sup>-1</sup> remains. The peaks at ~1900 and ~2025 cm<sup>-1</sup> on the freshly synthesized catalysts are attributed to bridge bonded CO on Rh of oxidation state 0 and 1, respectively. The peaks observed after calcination can similarly be attributed to linearly bound CO to Rh of oxidation state 0 (~2070 cm<sup>-1</sup>) or 1 (~2100 cm<sup>-1</sup>) and after reduction only linear bound CO on zero valent Rh is present.<sup>47-53</sup> This change in available binding sites is schematically represented in Figure 8(A).



One interesting discrepancy between these samples and conventionally prepared Rh/SiO<sub>2</sub> or Rh/Al<sub>2</sub>O<sub>3</sub> catalysts is that the CO peaks observed are drastically different. For conventionally prepared catalysts, bridge and atop CO are observed, but also peaks at ~2100 and ~2025 cm<sup>-1</sup> corresponding to the symmetric and antisymmetric stretches of rhodium gem-dicarbonyl, which entails two CO molecules adsorbed to a single Rh(I) atom<sup>31,47,48</sup>. This type of CO adsorption occurs only on isolated Rh atoms (not on NPs); the absence of these peaks in our spectra attest to the fact that all Rh exists on the support in NP form without any isolated Rh atoms. Such an observation strengthens the argument that colloidal synthesis produces NPs with low particle size distribution: atomically dispersed Rh is absent from these catalysts.

### 3.5 Comparison of infrared results and catalytic activity

The size dependence of CO oxidation over Rh NPs is lost after high temperature O<sub>2</sub> treatment followed by high temperature H<sub>2</sub> treatment. No change in particle size was observed by TEM after calcination (Figure 3), which leads us to speculate that the change in size dependence for CO oxidation is a result of decomposition of the stabilizing polymer PVP and/or the templating surfactant P123. It is difficult to characterize the nature of the polymers at the Pt interface because of the large excess of P123

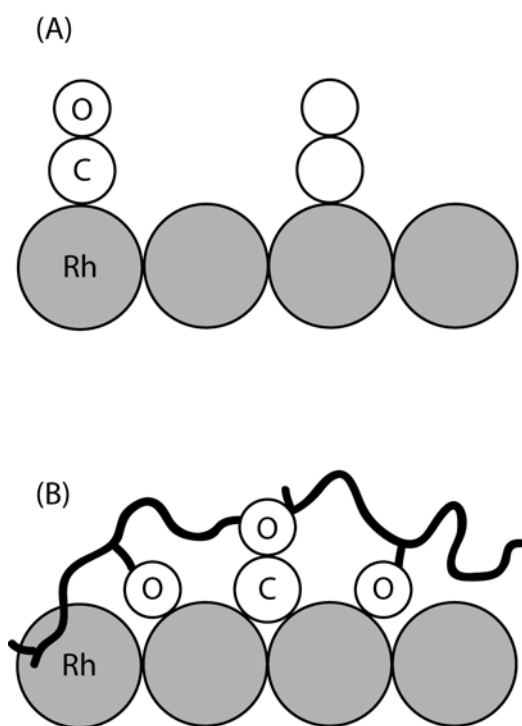
within the support that is not in close proximity to Pt NPs as well as the changes that occur to SBA-15, such as formation or decomposition of surface silanols. Instead, we have used CO as a probe molecule to characterize changes at or near the Pt surface.

There is a clear transformation in CO adsorption sites before and after different pretreatments. For the as-synthesized catalysts (no pretreatment), CO preferentially adsorbs to bridge sites on Rh with contribution from adsorption sites in at least two different chemical environments (Figure 8). In previous work, these sites have been attributed to bonding at Rh sites of valence 0 and 1.<sup>51</sup> After calcination in O<sub>2</sub>, CO adsorbs at atop sites on Rh(0) and Rh(I). Subsequent to *in situ* H<sub>2</sub> reduction, all Rh is converted to Rh(0) and only atop CO on Rh(0) is observed. One major question in this case is if/how this change in adsorption changes the reaction rate and bestows structure sensitivity to the reaction.

For the calcined and reduced catalysts, it appears that atop CO on Rh(0) sites reacts with surface oxygen in a fashion that is structure insensitive, while the reaction between bridge bound CO and surface oxygen is structure sensitive. Additionally, the uncalcined samples, on which CO adsorbs at bridge sites, exhibit higher catalytic activity. In this study, the uncalcined samples are most active, followed by the calcined and reduced samples; the calcined samples without reduction were least active for CO oxidation (data not shown). *In situ* infrared studies of CO oxidation over supported Rh catalysts have demonstrated that *gem*-dicarbonyl CO species, which form on isolated Rh(I) sites, are inactive for oxidation by O<sub>2</sub>, while atop and bridge CO species are both active.<sup>31,32,47</sup> In one study, it was proposed that CO adsorbed at Rh(0) sites is most active,<sup>32</sup> while in another it was proposed to be atop CO adsorbed at Rh(I) sites.<sup>31</sup> In our study, comparing the infrared spectra to CO oxidation results, bridge sites are most active, followed by atop CO adsorbed at Rh(0) sites and then atop CO adsorbed at Rh(I) sites.

The high activity endowed by the CO adsorbed on bridge sites may be influenced by the presence of intact PVP stabilizer in as-synthesized Rh/SBA-15. In as-synthesized samples, the carbonyl group in the pyrrolidone ring of PVP interacts with Rh atoms, stabilizing higher oxidation states of Rh and

changing the predominant mode of CO adsorption from atop to bridge sites (Figure 9). The reaction between O<sub>2</sub> and atop CO is independent of particle size and the reaction rate for Rh NP catalysts is similar to that over Rh single crystals.<sup>34</sup> The reaction rate of bridge CO with O<sub>2</sub>, however, appears to be particle size dependent. Thus, PVP “imposes” a particle size dependent rate on the Rh nanoparticles by altering the adsorption behavior of CO to favor bridge sites over atop sites. While this CO adsorption site appears to be more favorable (and size dependent), under these reaction conditions CO desorption is still rate limiting, as suggested by the -1 reaction order and the activation energy.<sup>54</sup>



Using DFT calculations, Gong *et al.* demonstrated that metal oxides are more active for CO oxidation than the corresponding metal surface as a result of the change in adsorption geometry of O adatoms that participate in the reaction. Specifically, they demonstrated that the reaction barrier for atop CO and atop O to react on an oxide surface is lower than the barrier for reaction between atop CO and bridge O on a metallic surface.<sup>55</sup> In our study, it appears that PVP alters the binding geometry of CO to the Rh surface. If O adatoms are adsorbed at bridge sites in both cases, then shifting CO adsorption from atop sites to bridge sites would provide a geometrically advantageous setup for reaction between CO and O adatoms.

The induced structure sensitivity may arise from two different sources. In our previous work, we demonstrated that smaller PVP capped Rh NPs are more oxidized during CO oxidation than larger particles.<sup>43</sup> This increased oxidation may give rise to a larger percentage of more active surfaces (i.e. the more active oxide surface studied by Gong *et al.*). A second possible explanation arises from the infrared spectroscopy presented here. CO adsorbed at bridge sites may be more influenced by the particle size than atop CO, which involves a single surface Rh atom.

#### **4. Conclusions**

We have described the synthesis, characterization, and catalytic properties for CO oxidation of a series of PVP stabilized Rh NPs between 1.9 and 11.3 nm supported on mesoporous SiO<sub>2</sub>. The synthesis of Rh NPs of narrow size distribution allows for careful studies of particle size effects in catalysis; this study demonstrates a complicating, but perhaps useful, issue in the use of colloiddally prepared NPs for catalytic applications. Having studied this series of PVP stabilized Rh NP catalysts before and after calcination in O<sub>2</sub> at ~ 623 - 723 K, we have concluded that (1) uncalcined PVP stabilized Rh NP catalysts exhibit a higher TOF for CO oxidation than calcined-reduced catalysts, (2) CO oxidation TOF increases with decreasing particle size for uncalcined catalysts, but CO oxidation is particle size independent for calcined-reduced catalysts, and (3) CO adsorbs at bridge sites before the catalysts are calcined, but on atop sites after calcination, with or without reduction in H<sub>2</sub>. By comparing infrared studies to TOF measurements for CO oxidation, we propose that PVP affects how CO binds to Rh and thus affects the TOF for CO oxidation. The presence of intact PVP results in preferential adsorption of CO at bridge sites, which causes an increase in catalytic activity as well as the observed particle size dependence for CO oxidation.

#### **Acknowledgements**

This work was supported by the Director, Office of Science, Office of Basic Energy Sciences, Division of Chemical Sciences, Geological and Biosciences of the U.S. Department of Energy under Contract No. DE-AC03-76SF00098. This work was also supported by the Director, Office of Science,

Office of Basic Energy Sciences, Division of Materials Sciences and Engineering of the U.S. Department of Energy under Contract No. DE-AC02-05CH11231. We would like to thank Tim Davenport for TGA-DSC measurements. TEM measurements were performed at the Robert D. Ogg Electron Microscope Lab at UC Berkeley. M.E.G. recognizes financial assistance as an Advanced Light Source Postdoctoral Fellow. Y.W.Z. appreciates the financial aid of Huaxin Distinguished Scholar Award from Peking University Education Foundation of China.

**Figure 1.** TEM images of (A) Rh(1.9 nm), (B) Rh(2.4 nm), (C) Rh(3.6 nm), (D) Rh(5.1 nm), (E) Rh(6.7 nm), and (F) Rh(11.3 nm). The large (> 5 nm) particles show well defined facets. The scale for all images is the same.

**Figure 2.** X-ray diffractograms of (A) Rh(1.9 nm), (B) Rh(1.9 nm)<sub>a</sub>, (C) Rh(2.4 nm), (D) Rh(3.6 nm), (E) Rh(5.1 nm), (F) Rh(6.7 nm), and (G) Rh(11.3 nm). The 111 diffraction peak broadens as the particle size decreases, consistent with the Scherrer equation. For the smallest particles, only the 111 reflection is sharp enough to resolve.

**Figure 3.** TEM images of calcined Rh nanoparticle catalysts, (A) Rh(1.9 nm)/SBA-15-c, (B) Rh(2.4 nm)/SBA-15-c, (C) Rh(6.7 nm)/SBA-15-c, and (D) Rh(11.3 nm)/SBA-15-c. While the particles tend to bunch together in certain regions, the particles do not agglomerate even after the high temperature calcination. The arrows indicate the location of Rh NPs on the SBA-15 support.

**Figure 4.** X-ray diffractograms of (A) Rh(11.3 nm), (B) Rh(11.3 nm)/SBA-15, (C) Rh(11.3 nm)/SBA-15-c before reduction, (D) Rh(11.3 nm)/SBA-15-c after reduction, and (E) Rh(11.3 nm)/SBA-15-c after CO oxidation indicate that the structure of the Rh(11.3 nm) nanoparticles is maintained after encapsulation, but calcination results in the formation of an amorphous Rh oxide. The Rh fcc structure is again observed upon subsequent reduction or reaction.

**Figure 5.** Combined (A) thermogravimetric analysis and (B) differential thermal analysis of (i) SBA-15, (ii) Rh(1.9 nm)/SBA-15, (iii) Rh(5.1 nm)/SBA-15, and (iv) Rh(11.3 nm)/SBA-15. The major weight loss (~15% of total weight) is due to decomposition of the templating surfactant and is similar for pure SBA-15 and for Rh(X)/SBA-15.

**Figure 6.** Arrhenius plots for (A) Rh(X)/SBA-15 and (B) Rh(X)/SBA-15-c, X = 1.9 nm (■), 1.9 nm<sub>a</sub> (□), 2.4 nm (▲), 3.6 nm (Δ), 5.1 nm (●), 6.7 nm (○), and 11.3 nm (×). The overall rate of reaction is

higher for the uncalcined samples, Rh(X)/SBA-15 series of catalysts. The activation energy for all samples is similar. The partial pressures of the reactants are 40 Torr CO and 100 Torr O<sub>2</sub>.

**Figure 7.** Turnover frequency as a function of particle size for Rh(X)/SBA-15 (as-synthesized) and Rh(X)/SBA-15-c (calcined and reduced). The reaction conditions are 443 K, 40 Torr CO, and 100 Torr O<sub>2</sub>.

**Figure 8.** DRIFTS of CO adsorbed on Rh catalysts with (A) a schematic of the binding of CO to Rh after different pretreatments, and infrared spectra of CO at room temperature on (B) Rh(1.9 nm)/SBA-15, (C) Rh(2.4 nm)/SBA-15, and (D) Rh(6.7 nm)/SBA-15.

**Figure 9.** Schematic representation of (A) atop CO on clean Rh nanoparticles and (B) bridge CO on PVP capped Rh nanoparticles.

**Scheme 1.** Structure of poly(vinylpyrrolidone) (PVP).

**Table 1:** Synthetic conditions for Rh nanoparticles

Sample	Rh(acac) <sub>3</sub> (mM)	PVP (mM)	Na Citrate (mM)	Butanediol (mL)	Final Temp (K)	TEM Size (nm)
Rh(1.9 nm)	5	50	15	40	493	1.9 ± 0.3
Rh(1.9 nm)a	5	50	5	40	493	1.9 ± 0.3
Rh(2.4 nm)	5	50	1.25	40	493	2.4 ± 0.4
Rh(3.6 nm)	5	50	0.5	40	493	3.6 ± 0.6
Rh(5.1 nm)	5	50	0.25	40	493	5.1 ± 0.7
Rh(6.7 nm)	1.25	12.5	0	120	498	6.7 ± 0.7
Rh(11.3 nm)	5	50	0	40	478	11.3 ± 1.6

**Table 2:** Characterization of Rh in calcined catalysts

Sample	Calcination Procedure	% Rh (ICP-OES)	Chemisorption <sup>a</sup>		Theoretical Dispersion (TEM) <sup>b</sup>
			H/Rh	CO/Rh	
Rh(1.9 nm)/SBA-15-c	24 h, 623 K	0.73	0.49	0.29	0.65
Rh(1.9 nm)a/SBA-15-c	24 h, 623 K	0.78	0.49	0.31	0.65
Rh(2.4 nm)/SBA-15-c	24 h, 623 K	0.78	0.48	0.29	0.51
Rh(3.6 nm)/SBA-15-c	24 h, 723 K	0.77	0.23	0.11	0.34
Rh(5.1 nm)/SBA-15-c	24 h, 723 K	0.53	0.13	0.02	0.24
Rh(6.7 nm)/SBA-15-c	36 h, 723 K	0.84	0.16	0.03	0.18
Rh(11.3 nm)/SBA-15-c	36 h, 723 K	0.82	0.11	0.04	0.11

<sup>a</sup> Room temperature chemisorption was measured after ex situ calcination followed by *in situ* H<sub>2</sub> reduction at 623 K for 1.5 h and 1 h evacuation at the same temperature. H/Rh and CO/Rh ratios are calculated using gas uptake and the Rh loading from ICP-OES.

<sup>b</sup> Theoretical dispersion calculated using TEM particle size assumes spherical particles.

**Table 3:** Summary of catalytic results for CO oxidation

Sample	Apparent $E_a$ (kcal/mol) <sup>a</sup>		TOF (s <sup>-1</sup> ) <sup>b</sup>	
	Uncalcined	Calcined	Uncalcined	Calcined
Rh foil				0.035
Rh(1.9 nm)/SBA-15	29.8 ± 0.3	28.8 ± 0.6	1.52	0.26
Rh(1.9 nm)a/SBA-15	30.0 ± 0.6	30.0 ± 1.0	1.69	0.38
Rh(2.4 nm)/SBA-15	26.8 ± 0.4	31.8 ± 1.6	0.94	0.13
Rh(3.6 nm)/SBA-15	26.1 ± 0.7	28.6 ± 0.5	0.65	0.30
Rh(5.1 nm)/SBA-15	29.1 ± 0.3	27.4 ± 2.7	0.47	0.06
Rh(6.7 nm)/SBA-15	27.4 ± 0.4	31.3 ± 1.2	0.63	0.11
Rh(11.3 nm)/SBA-15	30.2 ± 0.7	28.7 ± 0.2	0.39	0.22

<sup>a</sup> Determined at 40 Torr CO, 100 Torr O<sub>2</sub>, 423 – 523 K

<sup>b</sup> Determined at 40 Torr CO, 100 Torr O<sub>2</sub>, 443 K and calculating the number of surface sites from TEM and ICP-OES.

## References

- (1) Aiken, J. D.; Finke, R. G. *J. Mol. Catal. A: Chem.* **1999**, *145*, 1.
- (2) Gniewek, A.; Trzeciak, A. M.; Ziolkowski, J. J.; Kepinski, L.; Wrzyszczyk, J.; Tylus, W. *J. Catal.* **2005**, *229*, 332.
- (3) Jiang, Y. J.; Gao, Q. M. *J. Am. Chem. Soc.* **2006**, *128*, 716.
- (4) Li, Y.; Boone, E.; El-Sayed, M. A. *Langmuir* **2002**, *18*, 4921.
- (5) Li, Y.; Hong, X. M.; Collard, D. M.; El-Sayed, M. A. *Org. Lett.* **2000**, *2*, 2385.
- (6) Narayanan, R.; El-Sayed, M. A. *J. Am. Chem. Soc.* **2003**, *125*, 8340.
- (7) Pellegatta, J. L.; Blandy, C.; Colliere, V.; Choukroun, R.; Chaudret, B.; Cheng, P.; Philippot, K. *J. Mol. Catal. A: Chem.* **2002**, *178*, 55.
- (8) Porta, F.; Prati, L.; Rossi, M.; Coluccia, S.; Martra, G. *Catal. Today* **2000**, *61*, 165.
- (9) Rioux, R. M.; Song, H.; Hoefelmeyer, J. D.; Yang, P.; Somorjai, G. A. *J. Phys. Chem. B* **2005**, *109*, 2192.
- (10) Shiraishi, Y.; Toshima, N. *J. Mol. Catal. A: Chem.* **1999**, *141*, 187.
- (11) Stowell, C. A.; Korgel, B. A. *Nano Lett.* **2005**, *5*, 1203.
- (12) Venezia, A. M.; Liotta, L. F.; Pantaleo, G.; La Parola, V.; Deganello, G.; Beck, A.; Koppány, Z.; Frey, K.; Horvath, D.; Gucci, L. *Appl. Catal. A: Gen.* **2003**, *251*, 359.
- (13) Wan, B. S.; Liao, S. J.; Xu, Y.; Yu, D. R. *J. Mol. Catal. A: Chem.* **1998**, *136*, 263.
- (14) Zuo, X. B.; Liu, H. F.; Guo, D. W.; Yang, X. Z. *Tetrahedron* **1999**, *55*, 7787.
- (15) Lee, H.; Habas, S. E.; Kweston, S.; Butcher, D.; Somorjai, G. A.; Yang, P. *Angew. Chem. Int. Ed.* **2006**, *45*, 7824.
- (16) Li, Y.; El-Sayed, M. A. *J. Phys. Chem. B* **2001**, *105*, 8938.
- (17) Borodko, Y.; Habas, S. E.; Koebel, M.; Yang, P. D.; Frei, H.; Somorjai, G. A. *J. Phys. Chem. B* **2006**, *110*, 23052.
- (18) Borodko, Y.; Humphrey, S. M.; Tilley, T. D.; Frei, H.; Somorjai, G. A. *J. Phys. Chem. C* **2007**, *111*, 6288.
- (19) Du, Y. K.; Yang, P.; Mou, Z. G.; Hua, N. P.; Jiang, L. *J. Appl. Poly. Sci.* **2006**, *99*, 23.
- (20) Song, H.; Rioux, R. M.; Hoefelmeyer, J. D.; Komor, R.; Niesz, K.; Grass, M.; Yang, P. D.; Somorjai, G. A. *J. Am. Chem. Soc.* **2006**, *128*, 3027.
- (21) Einaga, H.; Harada, M. *Langmuir* **2005**, *21*, 2578.
- (22) Grass, M. E.; Yue, Y.; Habas, S. E.; Rioux, R. M.; Teall, C. I.; Yang, P.; Somorjai, G. A. *J. Phys. Chem. C* **2008**, *112*, 4797.
- (23) Rioux, R. M.; Song, H.; Grass, M.; Habas, S.; Niesz, K.; Hoefelmeyer, J. D.; Yang, P.; Somorjai, G. A. *Top. Catal.* **2006**, *39*, 167.
- (24) Ma, J. H.; Reng, S. H.; Pan, D. H.; Li, R. F.; Xie, K. C. *React. Funct. Polym.* **2005**, *62*, 31.
- (25) Baraldi, A.; Gregoratti, L.; Comelli, G.; Dhanak, V. R.; Kiskinova, M.; Rosei, R. *Appl. Surf. Sci.* **1996**, *99*, 1.
- (26) Bowker, M.; Quo, Q.; Li, Y.; Joyner, R. W. *Catal. Lett.* **1993**, *18*.
- (27) Hopstaken, M. J. P.; Niemantsverdriet, J. W. *J. Chem. Phys.* **2000**, *113*, 5457.
- (28) Leible, F. M.; Murray, P. W.; Francis, S. M.; Thornton, G.; Bowker, M. *Nature* **1993**, *363*, 706.
- (29) Peden, C. H. F.; Goodman, D. W.; Blair, D. S.; Berlowitz, P. J.; Fisher, G. B.; Oh, S. H. *J. Phys. Chem.* **1988**, *92*, 1563.
- (30) Anderson, J. A.; Solymosi, F. *J. Chem. Soc., Faraday Trans.* **1991**, *87*, 3435.
- (31) Cavers, M.; Davidson, J. M.; Harkness, I. R.; Rees, L. V. C.; McDougall, G. S. *J. Catal.* **1999**, *188*, 426.
- (32) Kiss, J. T.; Gonzalez, R. D. *J. Phys. Chem.* **1984**, *88*, 898.

- (33) Newton; Dent, A. J.; Diaz-Moreno, S.; Fiddy, S. G.; Jyoti, B.; Evans, J. *Chem. Eur. J.* **2006**, *12*, 1975.
- (34) Oh, S. H.; Eickel, C. C. *J. Catal.* **1991**, *128*, 526.
- (35) Oh, S. H.; Fisher, G. B.; Carpenter, J. E.; Goodman, D. W. *J. Catal.* **1986**, *100*, 360.
- (36) Solymosi, F.; Pasztor, M. *J. Phys. Chem.* **1985**, *89*, 4789.
- (37) Van't Blik, H. F. J.; Van Zon, J. B. A. D.; Huizinga, T.; Vis, J. C.; Koningsberger, D. C.; Prins, R. *J. Phys. Chem.* **1983**, *87*, 2264.
- (38) Altman, E. I.; Gorte, R. J. *Surf. Sci.* **1988**, *195*, 392.
- (39) Nehasil, V.; Stara, I.; Matolin, V. *Surf. Sci.* **1997**, *377*, 813.
- (40) Nehasil, V.; Stara, I.; Matolin, V. *Surf. Sci.* **1996**, *352*, 305.
- (41) Nehasil, V.; Stara, I.; Matolin, V. *Surf. Sci.* **1995**, *333*, 105.
- (42) Nehasil, V.; Zafeiratos, S.; Ladas, S.; Matolin, V. *Surf. Sci.* **1999**, *433-435*, 215.
- (43) Grass, M. E.; Zhang, Y.; Butcher, D. R.; Park, J. Y.; Li, Y.; Bluhm, H.; Bratlie, K. M.; Zhang, T.; Somorjai, G. A. *Angew. Chem. Int. Ed.* **2008**, *47*, 8893.
- (44) Zhang, Y. W.; Grass, M. E.; Habas, S. E.; Tao, F.; Zhang, T. F.; Yang, P. D.; Somorjai, G. A. *J. Phys. Chem. C* **2007**, *111*, 12243.
- (45) Rioux, R. M.; Grass, M. E.; Somorjai, G. A. PVP Decomposition; University of California, Berkeley: Berkeley, 2008.
- (46) Chen, M. S.; Cal, Y.; Yan, Z.; Gath, K. K.; Axnanda, S.; Goodman, D. W. *Surf. Sci.* **2007**, *601*, 5326.
- (47) Anderson, J. A. *J. Chem. Soc., Faraday Trans.* **1991**, *87*, 3907.
- (48) Cavanagh, R. R.; Yates, J. T. *J. Chem. Phys.* **1981**, *74*, 4150.
- (49) Dubois, L. H.; Somorjai, G. A. *Surf. Sci.* **1980**, *91*, 514.
- (50) Harrod, J. F.; Roberts, R. W.; Rissmann, E. F. *J. Phys. Chem.* **1967**, *71*, 343.
- (51) Rice, C. A.; Worley, S. D.; Curtis, C. W.; Guin, J. A.; Tarrer, A. R. *J. Chem. Phys.* **1981**, *74*, 6487.
- (52) Solymosi, F.; Rasko, J.; Bontovics, J. *Catal. Lett.* **1993**, *19*, 257.
- (53) Yates, J. T.; Duncan, T. M.; Worley, S. D.; Vaughan, R. W. *J. Chem. Phys.* **1979**, *70*, 1219.
- (54) Gao, F.; McClure, S. M.; Cai, Y.; Gath, K. K.; Wang, Y.; Chen, M. S.; Guo, Q. L.; Goodman, D. W. *Surf. Sci.* **2009**, *603*, 65.
- (55) Gong, X. Q.; Liu, Z. P.; Raval, R.; Hu, P. *J. Am. Chem. Soc.* **2004**, *126*, 8.